Computational Materials Science 245 (2024) 113282

Contents lists available at ScienceDirect

Computational Materials Science

journal homepage: www.elsevier.com/locate/commatsci

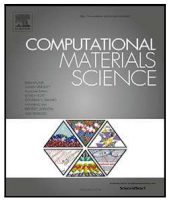

Full length article

Interfacial thermal conductance in 2D $WS_2/MoSe_2$ and $MoS_2/MoSe_2$ lateral heterostructures

Shihao Xu [a], Peichen Wu [b,*], Youping Chen [a]

[a] Department of Mechanical and Aerospace Engineering, University of Florida, Gainesville, FL 32611, USA
[b] Department of Materials Science and Engineering, Texas A&M University, 111J Reed McDonald Building, College Station, TX 77843, USA

ARTICLE INFO

Keywords:
Transition metal dichalcogenides
Interfacial thermal conductance
Molecular dynamics simulation
Interphase structure
Defect

ABSTRACT

In-plane Transition Metal Dichalcogenides (TMDs) heterostructures hold immense potential for various applications in the modern semiconductor industry, including electronics, optoelectronics, and photovoltaic devices. Different TMD monolayers can be 'stitched' together to construct an in-plane (lateral) heterostructure. As different TMD monolayers present different work functions and have their intrinsic shortcomings, a TMD heterostructure is an excellent form to optimize their properties and to achieve the best functionality. This requires a quantitative understanding of the properties of the interfaces in the heterostructures. In this work, we perform nonequilibrium molecular dynamics simulations, based on a parametrized Stillinger-Weber potential, to investigates the thermal conductance of the interfaces in 2D $WS_2/MoSe_2$ and $MoS_2/MoSe_2$ in-plane heterostructures, as well as in 2D lateral $WS_2/MoSe_2$ superlattices. Three distinct types of interfaces, including defect-free coherent interfaces, interfaces with the 5 | 7 defects, and the alloy-like incoherent interfaces, are explored. The effects of interphase structure and temperature are quantified. Phonon density of states (PDOS) analysis is used to understand the effect of different interphase structures. The effect of superlattice period on thermal conductance of the superlattices has also been quantified.

1. Introduction

Transition metal dichalcogenide (TMD) monolayers are part of the broader category of two-dimensional (2D) materials, renowned for their extraordinary thinness. Within the realm of 2D materials, TMDs play a crucial role by bridging the gap between conductive materials such as graphene and insulating materials like boron nitride. Monolayer TMDs are mechanically flexible and exhibit unique electronic and optical properties, which will be ideal candidates for next-generation optoelectronics. Monolayer TMDs also show promising thermoelectric property due to a high thermoelectric figure of merit ZT [1,2]. By using a two-dimensional ballistic transport model and first-principles density functional theory (DFT), Huang et al. studied the thermoelectric performance of a set of MX_2 type monolayers and p-type monolayer MoS_2 shows the highest value of ZT at room temperature [3–5].

Different monolayer transition metal dichalcogenides (TMDs) can be combined to create in-plane (lateral) heterostructures or stacked to form Van der Waals vertical heterostructures [6], as shown in Fig. 1. This study will only focus on in-plane heterostructures.

In-plane transition metal dichalcogenide (TMD) heterostructures hold significant merits for applications in the semiconductor industry, including electronics, optoelectronics, and photovoltaic devices. The ultra-thin and nanoscale structure of these materials presents a challenge in managing highly localized heat energy during the operation of TMD-based electronic devices [7]. Inadequate heat dissipation can profoundly impact the functionality of the nanodevices. The interfacial thermal conductance (ITC) within in-plane heterostructures not only influences the overall thermal conductivity of the whole structure [8] but also plays a crucial role in determining the interfacial thermal conductance between the heterostructure and its substrate in the TMDs-based device. Relatively high interfacial thermal conductance will benefit the heat dissipation of the nanodevice, thus achieving better performance. On the contrary, in-plane TMDs heterostructures with low interfacial thermal conductance can also be valuable, since the lower thermal conductivity within in-plane TMDs heterostructures can enhance the thermoelectric figure of merit (ZT) [9].

TMD lateral heterostructures, such as MoS_2/WS_2, $MoS_2/MoSe_2$, $WS_2/MoSe_2$, and MoS_2/WSe_2, have been successfully synthesized by using chemical vapor deposition (CVD) growth methods. Researchers have achieved smooth interfaces in lateral heterostructures through one-step and two-step CVD growth techniques [10–12], resulting in well-defined atomic interfaces. Additionally, Xie et al. performed a

* Corresponding author.
E-mail address: peichenw@tamu.edu (P. Wu).

https://doi.org/10.1016/j.commatsci.2024.113282
Received 19 June 2024; Received in revised form 30 July 2024; Accepted 4 August 2024
Available online 19 August 2024

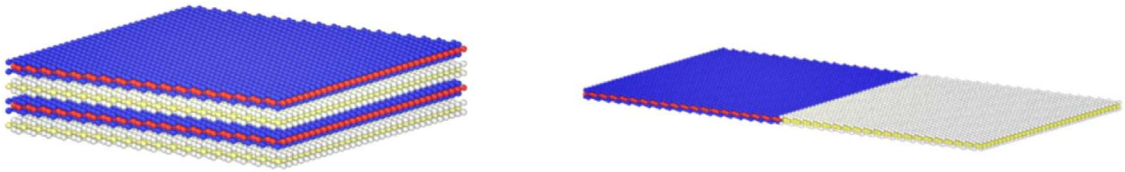

Fig. 1. Examples of vertical (out-of-plane) and lateral TMDs heterostructure.

modulated metal–organic chemical vapor deposition (MOCVD) process, also called omnidirectional epitaxy, to grow 2D TMDs superlattices with coherent interfaces, which means there are no dislocations at the interfaces despite the difference of lattice constants between each TMD [13]. Zhang et al. designed a step-by-step thermal CVD growth method called robust epitaxial growth, and they successfully synthesized 2D $WS_2/MoSe_2$, $WSe_2/MoSe_2$, WS_2/MoS_2, WSe_2/MoS_2, $WS_2/MoSe_2/WSe_2$, $WS_2/WSe_2/MoS_2$, $WS_2/MoS_2/WS_2$, and $WS_2/WSe_2/MoS_2$. These engineered heterostructures hold great potential for applications in various fields due to their tailored properties [14].

Experiment studies reveal that interfaces in in-plane transition metal dichalcogenide (TMD) heterostructures exhibit a diverse range of smoothness and sharpness, spanning from approximately 120 nm to as fine as 0.85 nm. Gong et al. fabricated in-plane WS_2/MoS_2 with an atomically sharp interface and 2 nm roughness using the chemical vapor deposition (CVD) method [15]. By using physical vapor transport and high-resolution scanning electron microscope, Huang et al. observed 10 nm alloy-like interface in the lateral WSe2/MoSe2 heterostructure [16].

To date, the work accomplished by Xie et al. stands as the sole reported successful synthesis of 2D TMD heterostructures with coherent interfaces and complete lattice coherence throughout the materials. Interestingly, out-of-plane ripples were observed in the WSe_2 region, which has a larger lattice constant compared to WS_2. According to the thin plate theory, in order to maintain a coherent interface without dislocations, the out-of-plane ripples need to be present to release the misfit strain at the interface. As a result of the coherence of the interfaces, the optical properties of the TMD devices have a broad range of tuning, and the photoluminescence peak shows 250 millielectron volts [13].

Additionally, a distinctive interface configuration, the 5 | 7 incoherent interface, was identified in 2D TMD heterostructures due to the relatively large lattice constant mismatch between the two TMDs. Zhou et al. found that the 5 | 7 misfit dislocations at the interface of 2D lateral WS_2/WSe_2 heterostructures serve as motivators for inducing the growth of sub-2-nm quantum-well arrays. These grown quantum wells have the potential to be used as a “conduit” of conductive nanoribbons, which can be further used in future 2D integrated circuits [17]. Han et al. also observed a similar growth mechanism in 2D lateral MoS_2/WSe_2 heterostructures, where sub-nanometer-wide MoS_2 grew into the WSe_2 region along the 5 | 7 misfit dislocations at the interface. The grown of 1D channels showed promise electronic properties that offer great potential applications in the future nano-electronic devices [18].

The main objective of this work is to quantify the thermal transport properties of the three types of interphase structures: the coherent interface, the 5 | 7 incoherent interface, and the alloy-like interface. This paper is organized as follows. After the introduction, Section 2 introduces the computational models, the Non-Equilibrium Molecular Dynamics (NEMD) and the method to measure the interface ITC. Section 3 reports simulation results, including the equilibrium heterostructures of $WS_2/MoSe_2$ and $MoS_2/MoSe_2$, interfacial thermal conductance of the three different interfacial structures, the effect of background temperature on ITC, and the effect of superlattice period on the thermal conductance of the superlattice. This section also includes an examination of the morphology of a $WS_2/MoSe_2$ superlattice structure. Section 4 presents major conclusions of this work.

2. Methods

2.1. Computer models of 2D $WS_2/MoSe_2$ and $MoS_2/MoSe_2$

Atomic level computer models for three types of interfaces in 2D $WS_2/MoSe_2$ and $MoS_2/MoSe_2$ in-plane heterostructures are presented in Fig. 2. In this work, a coherent interface means that the interface is atomically sharp and defect free. The 5 | 7 incoherent interface refers to an interface having 5- and 7- fold rings. The alloy-like incoherent interface describes an interface exhibiting a random alloy-like configuration.

All the simulated structures have the same dimension of 80.7×62.0 nm^2 for the length and width. In Fig. 2, the top row illustrates the ideal configurations of heterostructures with coherent interfaces. In this arrangement, WS_2, MoS_2, and $MoSe_2$ are constructed with an identical lattice constant of 3.21 Å. The middle row of Fig. 2 displays the configurations of heterostructures with 5 | 7 incoherent interfaces. Here, WS_2, MoS_2, and $MoSe_2$ are constructed with their respective lattice constants of 3.13 Å, 3.16 Å, and 3.29 Å. The bottom row in Fig. 2 shows the configurations of heterostructures with alloy-like incoherent interfaces. In this case, WS_2, MoS_2, and $MoSe_2$ are constructed with a consistent lattice constant of 3.21 Å, and the interface adopts a random alloy-like configuration with a width of 2 nm.

Because the material systems in this study are in nanoscale, so the molecular dynamics simulation is the most suitable simulation tool. If the dimension of the material system rises to the mesoscale, the Concurrent Atomistic-Continuum (CAC) [19–22] method and phase field method [23,24] can also be considered. The thermal properties analyzed in this paper can serve as a database for machine learning, facilitating the design of metamaterials with tailored functionality [25,26]. Well tested force field parametrizations for the materials are well available, thus classical molecular dynamics (MD) simulation is used for this study. However, for 2D materials incorporating heavier elements such as In and Bi, where the corresponding force field parametrizations are less tested or absent in MD simulations of 2D structures, ab initio molecular dynamics (AIMD) simulations is recommended. AIMD extends the scope of classical MD methodologies to 2D materials obtained from MOCVD/CVD processes without detracting from the applicability and adequacy of classical MD simulations [27,28].

2.2. Non-equilibrium molecular dynamics

To compute the interfacial thermal conductance of $WS_2/MoSe_2$ and $MoS_2/MoSe_2$ in-plane heterostructures with coherent, 5 | 7 incoherent, and alloy-like incoherent interfaces, the nonequilibrium molecular dynamics (NEMD) method was employed. In this method, a heat source was positioned at one end, and a heat sink was placed at the opposite end of each structure. The widths of both the heat source and heat sink were maintained at 3 nm. The schematic representation of the NEMD method employed in this study is presented in Fig. 3.

In this study, molecular dynamics simulations were conducted using LAMMPS [29]. A periodic boundary condition was implemented along the in-plane y-direction, while free-boundary conditions were employed along the in-plane x-direction and out-of-plane z-direction. The covalent interactions among Mo, W, S, and Se atoms were described using the parametrized Stillinger-Weber potential [30].

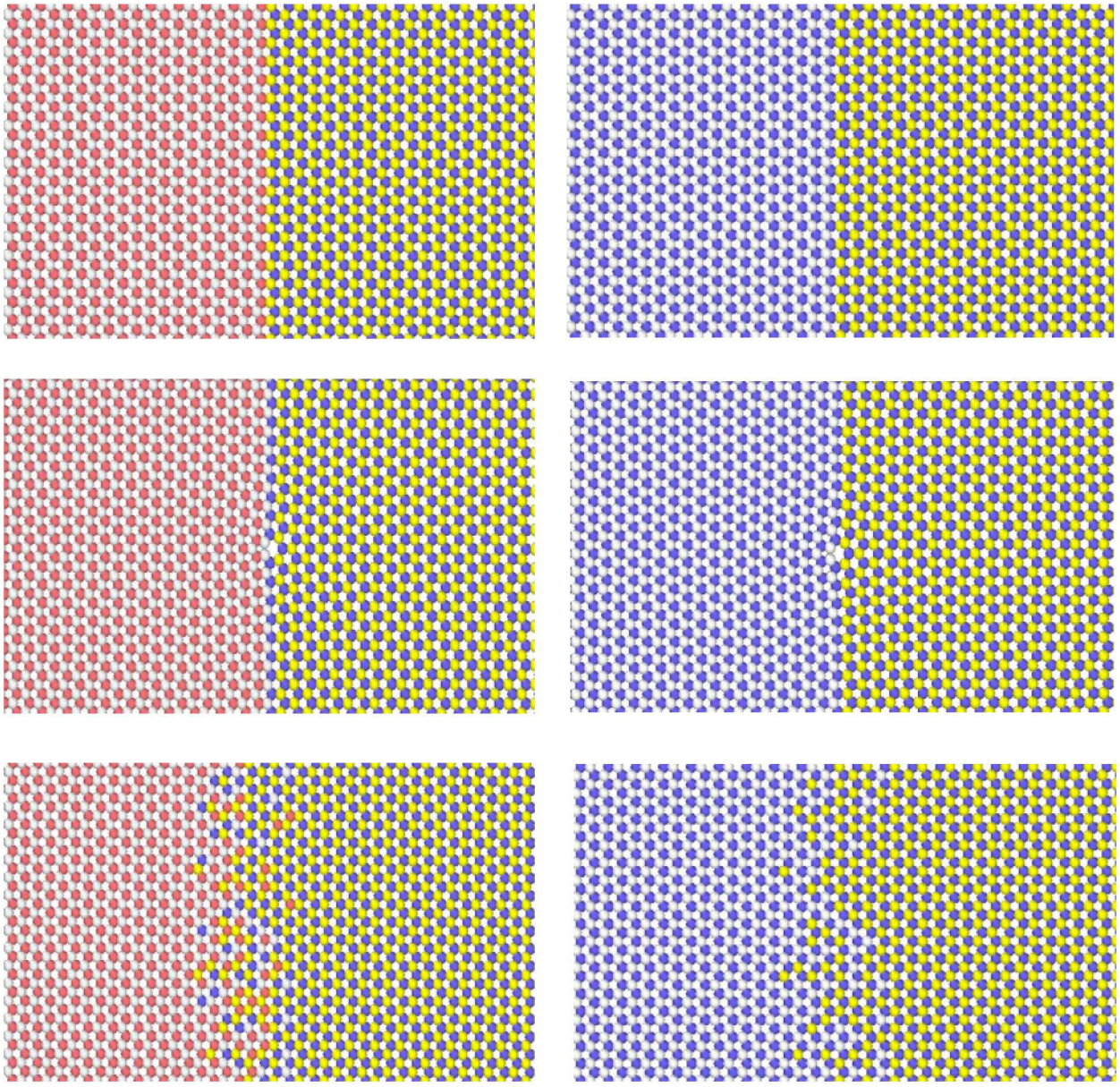

Fig. 2. Atomic level computer models of the 2D $WS_2/MoSe_2$ and $MoS_2/MoSe_2$ in-plane heterostructures are illustrated. In the first column, from top to bottom, are the WS2/MoSe2 heterostructures with coherent, 5 | 7 incoherent, and alloy-like incoherent interfaces, respectively. The second column, from top to bottom, features $MoS_2/MoSe_2$ heterostructures with coherent, 5 | 7 incoherent, and alloy-like incoherent interfaces, respectively. In these representations, W atoms are denoted in red, Mo atoms in blue, S atoms in white, and Se atoms in yellow.

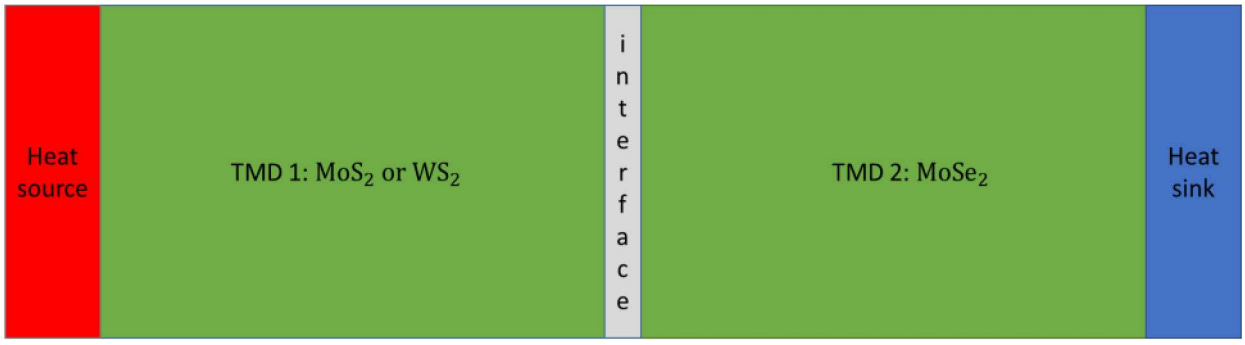

Fig. 3. The schematic of NEMD method, encompassing interfaces that can be coherent, 5 | 7 incoherent, and alloy-like incoherent.

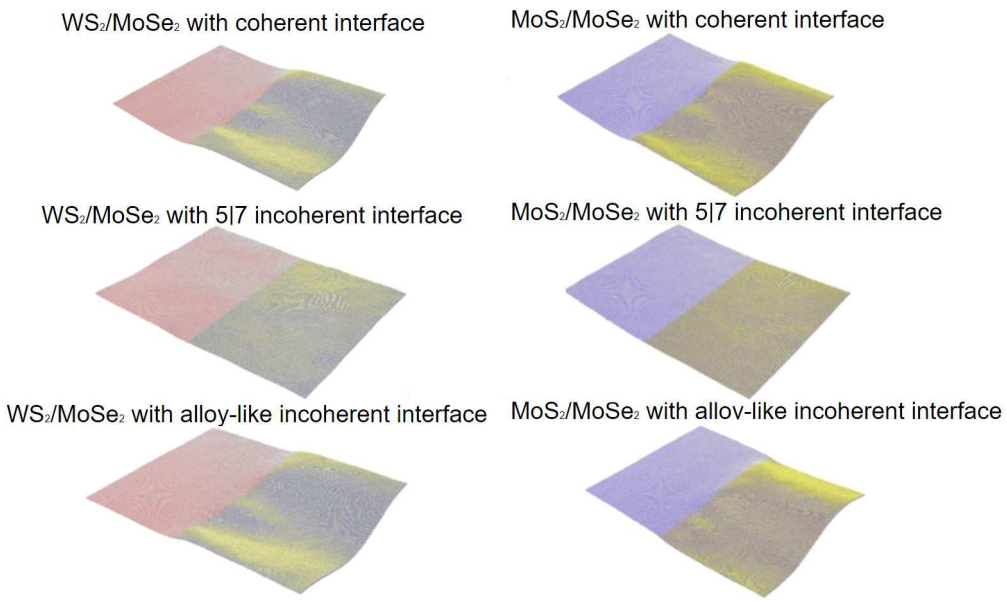

Fig. 4. The structure configurations of 2D lateral WS2/MoSe2 and MoS2/MoSe2 heterostructures with coherent, 5 | 7 incoherent, and alloy-like interfaces.

The velocity Verlet algorithm [31] was utilized to numerically integrate Newton's equations of atom motion, employing a time step of 1 fs. The initial step involved equilibrating the heterostructures to 300 K. Then, the temperatures at the heat source and heat sink regions were set to be 330 K and 270 K, respectively. Nonequilibrium molecular dynamics (NEMD) simulations were conducted for 5 ns to establish steady-state temperature gradients along the longitudinal x-direction. The final 1 ns of simulation results were utilized for the analysis of interfacial thermal conductance characteristics. The calculation of interfacial thermal conductance followed the equation:

$$\lambda = \frac{J}{\delta T} \tag{1}$$

,where λ is the interfacial thermal conductance, J is the heat flux across the interface, and δT is the temperature across the interface.

3. Results and discussion

3.1. Out-of-plane structural rippling

It is crucial to acknowledge that substantial out-of-plane structural rippling have emerged in the $WS_2/MoSe_2$ and $MoS_2/MoSe_2$ heterostructures with coherent and alloy-like incoherent interfaces during the MD simulations. These rippling resulted from misfit strain around the interfaces and the ultra-thin nature of the TMD layers. Importantly, the out-of-plane rippling remained structurally stable throughout the simulations, as illustrated in Fig. 4. In contrast, the heterostructures with 5 | 7 incoherent interfaces maintained a flat configuration throughout the simulations, as shown in Fig. 4.

3.2. Interfacial thermal conductance (ITC) of $WS_2/MoSe_2$ and $MoS_2/MoSe_2$ heterostructures at 300K

The interfacial thermal conductance calculation results are shown in the Table 1. At temperature of 300 K, the interfacial thermal conductance for lateral $WS_2/MoSe_2$ heterostructures with coherent interfaces is calculated to be 11.95×10^8 W/Km^2, which is slightly smaller than the ITC of $MoS_2/MoSe_2$ heterostructures, 12.85×10^8 W/Km^2. Notably, in both lateral $WS_2/MoSe_2$ and $MoS_2/MoSe_2$ heterostructures, configurations with coherent interfaces consistently exhibit the highest interfacial thermal conductance.

Within $WS_2/MoSe_2$ heterostructures, those with alloy-like incoherent interfaces display the lowest interfacial thermal conductance of 8.7×10^8 W/Km^2. In contrast, structures with 5 | 7 incoherent interfaces exhibit an interfacial thermal conductance of 9.17×10^8 W/Km^2.

Moving to $MoS_2/MoSe_2$ heterostructures, those with 5 | 7 incoherent interfaces has the lowest interfacial thermal conductance of 10.65×10^8 W/Km^2. Conversely, structures with alloy-like incoherent interfaces display an interfacial thermal conductance of 11.67×10^8 W/Km^2. It is noteworthy that at 300 K, the interfacial thermal conductance of $MoS_2/MoSe_2$ with all three types of interfaces are higher than that of $WS_2/MoSe_2$. The temperature profile and energy change between heat source and heat sink for each interface are shown in Fig. 6 and Fig. 5 respectively.

3.3. Background temperature effect on interfacial thermal conductance

Various background temperatures, **ranging from 200K to 500K**, were used in the simulations to investigate the temperature effect on interfacial thermal conductance. **These temperatures represent the typical temperature range in real applications**. Simulation results are presented in Table 1. Prior to the NEMD simulation tests, all models went through a relaxation process at the specified background temperature.

It is seen from Table 1 and Fig. 7, the interfacial thermal conductance increased with rising temperatures for lateral $WS_2/MoSe_2$ and $MoS_2/MoSe_2$ heterostructures with three different types of interfaces. However, for $WS_2/MoSe_2$ with the coherent interface, there was an exception at 500 K, where the conductance was smaller than that at 400 K. For all background temperatures studied, the interfacial thermal conductance of $MoS_2/MoSe_2$ with all three types of interfaces were higher than that of $WS_2/MoSe_2$.

3.4. Phonon density of states analysis of the three types of interfaces

To understand the effect of interphase structure on the interfacial thermal conductance of 2D lateral $WS_2/MoSe_2$ and $MoS_2/MoSe_2$ heterostructures, an analysis of the phonon density of states (PDOS) was conducted. It is widely recognized that in the 2D material system, the overlap of the PDOS of the materials or groups of atoms on the two sides of an interface provides insights into the thermal transportability

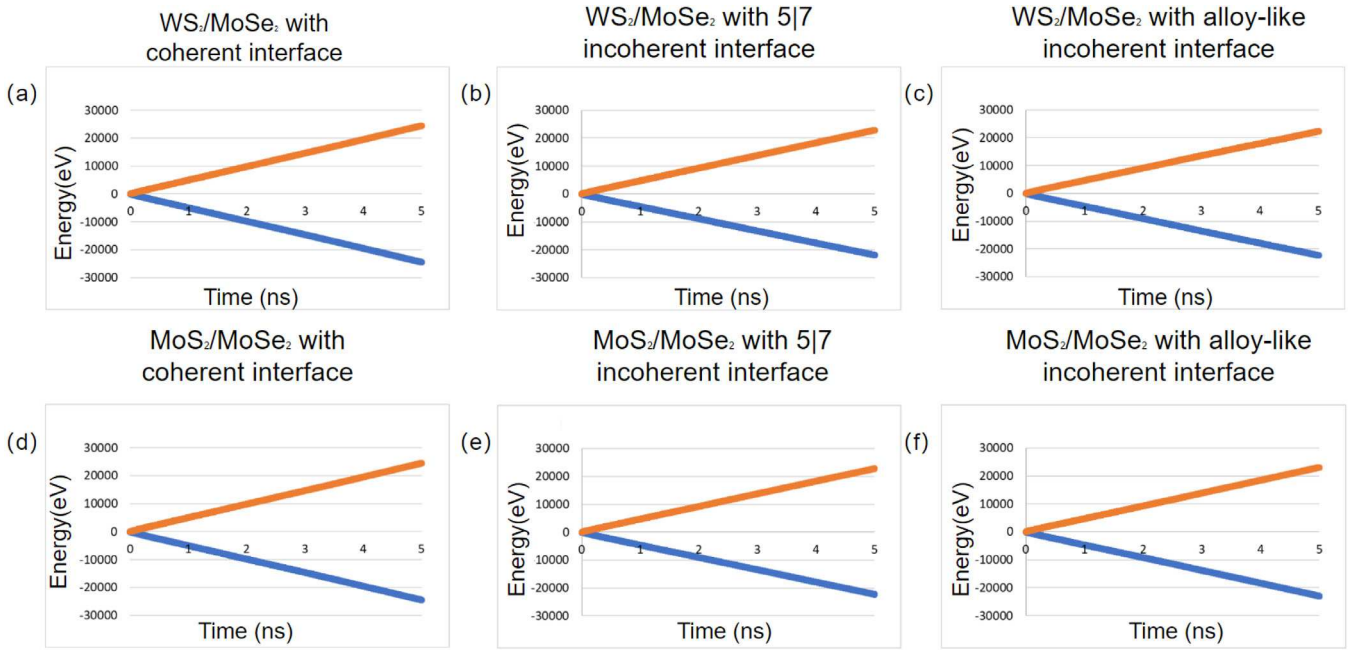

Fig. 5. Energy changes in heat source and heat sink of 2D lateral $WS_2/MoSe_2$ and $MoS_2/MoSe_2$ heterostructures.

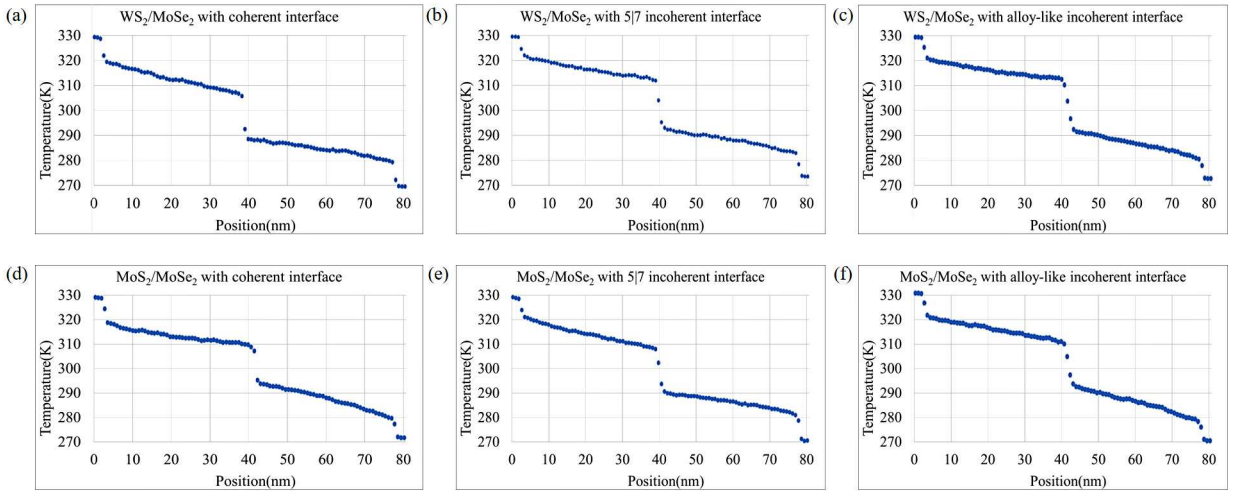

Fig. 6. Temperature profile of 2D lateral $WS_2/MoSe_2$ and $MoS_2/MoSe_2$ heterostructures.

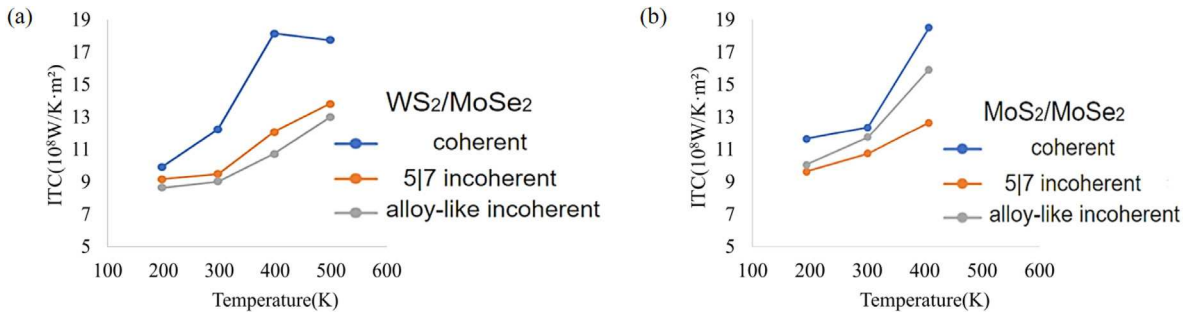

Fig. 7. Interfacial thermal conductance of $WS_2/MoSe_2$ and $MoS_2/MoSe_2$ heterostructures with different interface type.

Table 1
Interfacial thermal conductance of $WS_2/MoSe_2$ and $MoS_2/MoSe_2$ heterostructures at different background temperatures.

Interfacial thermal conductance (W/Km^2)					
Interface type	Material combination	200 K	300 K	400 K	500 K
Coherent	$WS_2/MoSe_2$	9.63×10^8	11.95×10^8	17.87×10^8	17.47×10^8
5 | 7 incoherent	$WS_2/MoSe_2$	8.86×10^8	9.17×10^8	11.77×10^8	13.51×10^8
alloy-like incoherent	$WS_2/MoSe_2$	8.32×10^8	8.7×10^8	10.43×10^8	12.7×10^8
Coherent	$MoS_2/MoSe_2$	11.57×10^8	12.85×10^8	18.5×10^8	not stable
5 | 7 incoherent	$MoS_2/MoSe_2$	9.53×10^8	10.65×10^8	12.59×10^8	not stable
alloy-like incoherent	$MoS_2/MoSe_2$	9.95×10^8	11.67×10^8	15.88×10^8	not stable

Table 2
PDOS overlapping for $WS_2/MoSe_2$ and $MoS_2/MoSe_2$ with three types of interface.

PDOS overlapping (S)		
Interface type	$WS_2/MoSe_2$	$MoS_2/MoSe_2$
Coherent	0.2193	0.2323
5 | 7 incoherent	0.1473	0.1637
alloy-like incoherent	0.1401	0.1710

Table 3
Thermal conductivity of $WS_2/MoSe_2$ superlattice with different periods.

Number of periods	Period length L_p (nm)	Thermal conductivity (W/Km)
3	83.3	44.476
4	62	45.803
5	50	45.002
10	25	42.664
20	12.5	39.893
25	10	39.055
30	8.3	43.242
50	5	41.477

across that interface. The PDOS overlapping can be quantified using the following equation:

$$S = \frac{\int_0^\infty D_{atom1}(w) D_{atom2}(w) dw}{\int_0^\infty D_{atom1} D_{atom2} dw} \quad (2)$$

Where, w represents the vibration frequency of a specific atom. The subscripts atom1 and atom2 denote the two types of atoms constituting the particular interface. In the case of $WS_2/MoSe_2$ heterostructures, atom 1 represents W atoms, and atom 2 represents Se atoms. Meanwhile, for $MoS_2/MoSe_2$ heterostructures, atom 1 corresponds to Mo atoms, and atom 2 corresponds to Se atoms.

In this investigation, Phonon Density of States (PDOS) analysis was performed for the atoms of the two distinct materials in the heterostructures Specifically, for 2D lateral $WS_2/MoSe_2$ heterostructures with coherent, 5 | 7 incoherent, and alloy-like incoherent interfaces, the PDOS analysis focused on the nearest W and Se atoms at the specific interface. Similarly, for 2D lateral $MoS_2/MoSe_2$ heterostructures with coherent, 5 | 7 incoherent, and alloy-like incoherent interfaces, the PDOS analysis concentrated on the nearest Mo and Se atoms at the specific interface.

The PDOS overlapping value can serve as an indicator of the heat transport capability across the interface. For heterostructures with different types of interfaces, a higher PDOS overlapping value signifies easier heat transfer across the interface, leading to a higher interfacial thermal conductance. Conversely, a lower PDOS overlapping value indicates a more challenging heat transfer across the interface, resulting in lower interfacial thermal conductance. For 2D lateral $WS_2/MoSe_2$ heterostructures, the PDOS overlapping for the coherent interface is 0.2193, for the 5 | 7 incoherent interface is 0.1473, and for the alloy-like incoherent interface is 0.1401. Similarly, for 2D lateral $MoS_2/MoSe_2$ heterostructures, the PDOS overlapping for the coherent interface is 0.2323, for the 5 | 7 incoherent interface is 0.1637, and for the alloy-like incoherent interface is 0.1710. Refer to Table 2 for the computed overlapping data. Fig. 8 presents the PDOS results.

3.5. Morphology and thermal conductance of single layer WS2/MoSe2 superlattice with coherent interface

The initial configurations for lateral 2D $WS_2/MoSe_2$ superlattices were created with varying numbers of periods: $3, 4, 5, 10, 20, 25, 30$ and 50. All the computer models have identical structural dimensions of 250 nm × 62.7 nm and the same coherent interface.

Notably, at temperature of 10K, as the number of periods increases, the characteristic ripple feature becomes less pronounced but remains discernible, as shown in Fig. 9. However, after thermalization of the structures to 300K, the regular ripple feature is absent in structures with more than 10 periods, as shown in Fig. 10. The corresponding temperature profile for different period length at a background temperature of 300K are shown in Fig. 11

2D materials display remarkable flexibility in response to out-of-plane deformation. Previous studies have shown that suspended graphene can undergo out-of-plane structural warping even under room temperature, and the same holds true for supported graphene on uneven substrates. Transition metal dichalcogenide (TMD) materials exhibit similar characteristics.

In the context of superlattices, an interface mismatch induces significant in-plane tensile strain in the WS_2 domain due to its smaller lattice constant, while the $MoSe_2$ lattice will experience stretching to form a coherent interface. Conversely, the $MoSe_2$ domain on the opposite side of the interface experiences compression. As a result, the superlattice tends to develop ripples, releasing the stress energy to attain a stable state.

The thermal conductances for different superlattices with different period length were calculated and shown in Table 3. Our simulation results have shown that the superlattice structure with a period length (L_p) of 25.0 nm displayed the lowest thermal conductivities 39.055 W/(Km). In contrast, the superlattice structure with L_p = 62.0 nm exhibited the highest thermal conductivities, reaching 45.803 W/(Km). These results indicate that both the periodic length and the ripples generated within the superlattice influence the its thermal conductivity of the superlattice.

4. Summary and conclusions

In this work, we have computed the interfacial thermal conductance (ITC) in 2D lateral $WS_2/MoSe_2$ and $MoS_2/MoSe_2$ heterostructures as a function of temperature. Three types of interphase structures, including (1) defect-free-coherent, (2) 5 | 7 incoherent interface, and (3) alloy-like incoherent interfaces, for each heterostructure were explored. Major findings are summarized as follows.

(1) Substantial out-of-plane structural rippling were observed in both $WS_2/MoSe_2$ and

$MoS_2/MoSe_2$ heterostructures with coherent and alloy-like incoherent interfaces. In contrast, heterostructures with 5 | 7 incoherent interfaces maintained a flat configuration due to the release of the misfit strain by the 5 | 7 defects. The ripple feature is also absent in superlattice structures with more than 10 periods.

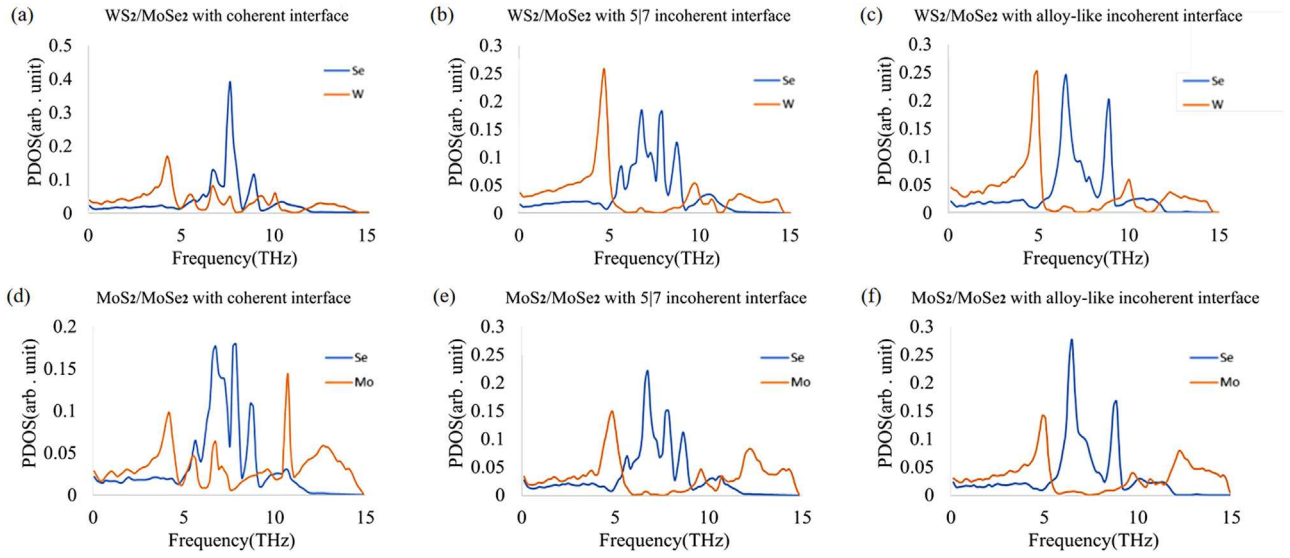

Fig. 8. PDOS of $WS_2/MoSe_2$ and $MoS_2/MoSe_2$ heterostructures with different interface type.

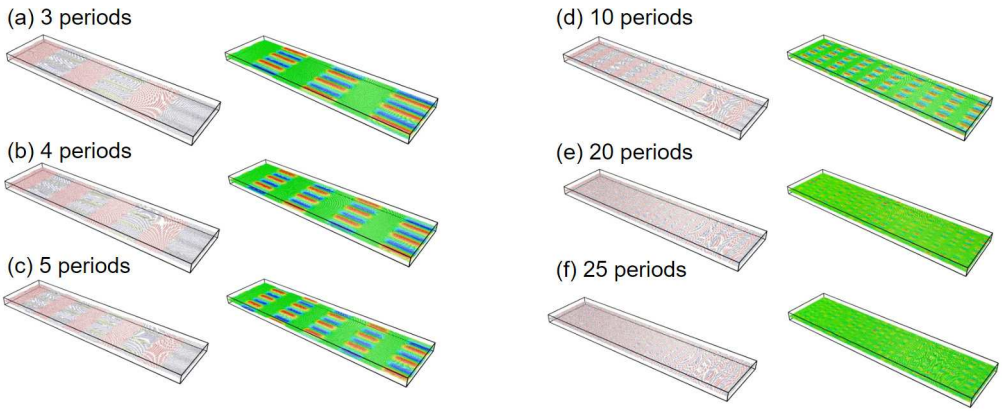

Fig. 9. Morphology of superlattices at T = 10 K. The images on the right side of each column depict the superlattices after the application of positional color coding along the *z*-direction (Red color indicates the highest position, while blue color indicates the lowest position.).

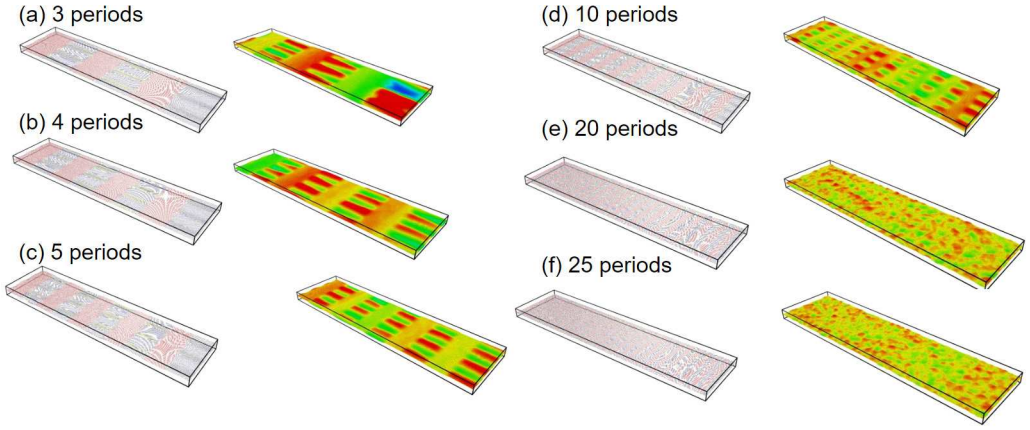

Fig. 10. Morphology of superlattices at T = 300 K. The images on the right side of each column depict the superlattices after the application of positional color coding along the *z*-direction (Red color indicates the highest position, while blue color indicates the lowest position.).

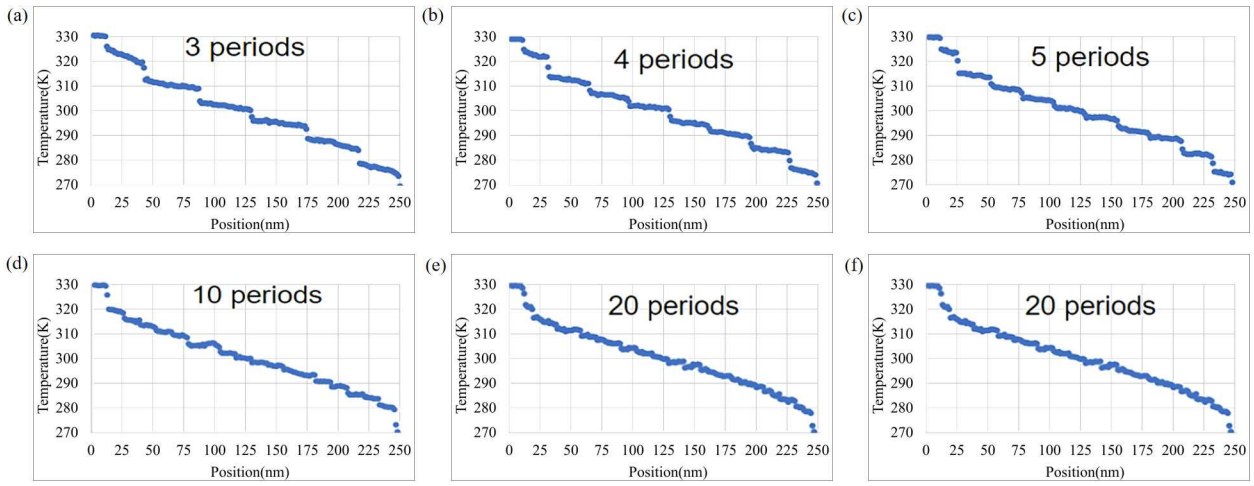

Fig. 11. Temperature profile between the heat source and sink were investigated for superlattices with 3, 5, 10, 20, 25, and 30 periods, respectively.

(2) For all heterostructures investigated in this work, the coherent interfaces were found to have the highest interfacial thermal conductance. In $WS_2/MoSe_2$ heterostructures, the alloy-like incoherent interface has the lowest interfacial thermal conductance. However, in $MoS_2/MoSe_2$ heterostructures, the 5 | 7 incoherent interface has the lowest interfacial thermal conductance.

(3) The interfacial thermal conductance was found to increase with temperature, except for the coherent interface in the $WS_2/MoSe_2$ heterostructure at 500 K, which was smaller than that at 400 K.

(4) To understand the different effects of interphase structure on ITC, phonon density of states (PDOS) was computed for each heterostructure. Calculation results confirmed that the PDOS overlapping value between the two different materials at the interface serves as an indicator of the heat transport capability across the interface in 2D materials, and the PDOS analysis results are consistent with the measured values of the ITCs for all the heterostructures.

(5) Both the length of periods and the ripples generated in the superlattice were found to be influential factors affecting thermal conductivity. Specifically, the $WS_2/MoSe_2$ superlattice structure with a period length of 10.0 nm demonstrated the lowest thermal conductivity of 39.055 W/(Km), while that with a period length of 62.0 nm exhibited the highest thermal conductivity of 45.803 W/(Km).

Thermal transport across interfaces in heterostructures is a complex process. This work has shown that similar interphase structure in different heterostructures may have different effects on thermal boundary conductance. Nevertheless, the overall effect of defects on the interface thermal conductance of in-plane transition metal dichalcogenides heterostructures found in this work is consistent with that found in other heterostructures, such as the GaN/AlN interphase [32] and the PbTe/PbSe interphase [33,34].

CRediT authorship contribution statement

Shihao Xu: Visualization, Validation, Methodology, Investigation, Formal analysis, Data curation, Conceptualization. **Peichen Wu:** Writing – review & editing, Writing – original draft, Methodology, Investigation. **Youping Chen:** Supervision, Conceptualization.

Declaration of competing interest

The authors declare that they have no known competing financial interests or personal relationships that could have appeared to influence the work reported in this paper.

Data availability

Data will be made available on request.

Acknowledgments

This work is based on research supported by the US National Science Foundation under Award Number CMMI-2054607. The computer simulations are funded by the Advanced Cyberinfrastructure Coordination Ecosystem: Services & Support (ACCESS) allocation TG-DMR190008.

References

[1] C. Kai-Xuan, W. Xiao-Ming, M. Dong-Chuan, L. Shu-Shen, Thermoelectric properties of transition metal dichalcogenides: From monolayers to nanotubes, J. Phys. Chem. C 119 (2015) 47.
[2] H. Wen, D. Haixia, L. Gengchiau, Thermoelectric performance of MX2 (M=Mo,W; X=S,Se) monolayers, J. Appl. Phys. 113 (2013) 104304.
[3] A. Lipatov, P. Sharma, A. Gruverman, A. Sinitskii, Optoelectrical molybdenum disulfide (MoS2) ferroelectric memories, ACS Nano 9 (8) (2015) 8089–8098.
[4] A. Castellanos-Gomez, M. Poot, G.A. Steele, H. van der Zant, N. Agraït, G. Rubio-Bollinger, Elastic properties of freely suspended MoS2 nanosheets, Adv. Mater. 24 (6) (2012) 772–775.
[5] R. Yan, J.R. Simpson, S. Bertolazzi, J. Brivio, M. Watson, X. Wu, A. Kis, T. Luo, A. Walker, H. Xing, Thermal conductivity of monolayer molybdenum disulfide obtained from temperature-dependent Raman spectroscopy, ACS Nano 8 (1) (2014) 986–993.
[6] M.Y. Li, C.H. Chen, Y. Shi, L.J. Li, Heterostructures based on twodimensional layered materials and their potential applications, Mater. Today 19 (6) (2016) 322–335.
[7] X. Liu, Y. Zhang, Thermal properties of transition-metal dichalcogenide, Chin. Phys. B 27 (3) (2018) 034402.
[8] Z. Ong, G. Zhang, Y. Zhang, Controlling the thermal conductance of graphene/h-BN lateral interface with strain and structure engineering, Phys. Rev. B 93 (7) (2016) 075406.
[9] G. Zhang, Y. Zhang, Thermoelectric properties of two-dimensional transition metal dichalcogenides, J. Mater. Chem. C 5 (31) (2017) 7684–7698.
[10] X. Duan, C. Wang, J.C. Shaw, R. Cheng, Y. Chen, H. Li, X. Wu, Y. Tang, Q. Zhang, A. Pan, J. Jiang, R. Yu, Y. Huang, X. Duan, Lateral epitaxial growth of two-dimensional layered semiconductor heterojunctions, Nature Nanotechnol. 9 (12) (2014) 1024.
[11] L. Tizei, Y. Lin, M. Mukai, H. Sawada, A. Lu, L. Li, K. Kimoto, K. Suenaga, Exciton mapping at subwavelength scales in two-dimensional materials, Phys. Rev. Lett. 114 (10) (2015) 107601.
[12] P. Chen, Z. Zhang, X. Duan, X. Duan, Chemical synthesis of twodimensional atomic crystals, heterostructures and superlattices, Chem. Soc. Rev. 47 (9) (2018) 3129–3151.
[13] S. Xie, L. Tu, Y. Han, L. Huang, K. Kang, K. Lao, P. Poddar, C. Park, D. Muller, R. Distasio, J. Park, Coherent, atomically thin transition-metal dichalcogenide superlattices with engineered strain, Science 359 (6380) (2018) 1131–1136.
[14] Z. Zhang, P. Chen, X. Duan, K. Zang, J. Luo, X. Duan, Robust epitaxial growth of two-dimensional heterostructures, multiheterostructures, and superlattices, Science 357 (6353) (2017) 788–792.
[15] Y. Gong, J. Lin, X. Wang, G. Shi, S. Lei, Z. Lin, H. Terrones, Vertical and in-plane heterostructures from WS2/MoS2 monolayers, Nat. Mater. 13 (12) (2014) 1135.

[16] C. Huang, S. Wu, A.M. Sanchez, J. Peters, R. Beanland, J. Ross, X. Xu, Lateral heterojunctions within monolayer MoSe2/WSe2 semiconductors, Nat. Mater. 13 (12) (2014) 1096.
[17] W. Zhou, Y.Y. Zhang, J. Chen, D. Li, J. Zhou, Z. Liu, K. Loh, Dislocation-driven growth of two-dimensional lateral quantum-well superlattices, Sci. Adv. 4 (3) (2018) 9096.
[18] Y. Han, M.Y. Li, G. Jung, M. Marsalis, Z. Qin, M. Buehler, L. Li, D. Muller, Sub-nanometer channels embedded in two-dimensional materials, Nat. Mater. 17 (2) (2018) 129.
[19] Y. Chen, J. Lee, Atomistic formulation of a multiscale field theory for nano/micro solids, Phil. Mag. 85 (4095–4126) (2005).
[20] Y. Chen, Reformulation of microscopic balance equations for multiscale materials modeling, J. Chem. Phys. 130 (134706) (2009).
[21] Y. Chen, S. Shabanov, D. McDowell, Concurrent atomistic-continuum modeling of crystalline materials, J. Appl. Phys. 126 (101101) (2019).
[22] A. Diaz, B. Gu, Y. Li, S. Plimpton, D. McDowell, Y. Chen, A parallel algorithm for the concurrent atomistic-continuum methodology, J. Comput. Phys. 463 (111140) (2022).
[23] R. Raghavan, P. Wu, K. Ankit, Phase-field modeling of nanostructural evolution in physical vapor deposited phase-separating ternary alloy films, Modelling Simul. Mater. Sci. Eng. 30 (8) (2022) 084004.
[24] M. Glicksman, P. Wu, K. Ankit, Surface Laplacian of interfacial thermochemical potential: its role in solid liquid pattern formation, Nat. Microgravity 7 (1) (2021) 41.
[25] W. Yuling, V. Vijay, L. Xiaochuan, M. Slava, Z. Qiang, H. Mingguo, Z. Song, Real-time excitation control-based voltage regulation using ddpg considering system dynamic performance, IEEE Open Access J. Power Energy 10 (643–653) (2023).
[26] P. Wu, A. Iquebal, K. Ankit, Emulating microstructural evolution during spinodal decomposition using a tensor decomposed convolutional and recurrent neural network, Comput. Mater. Sci. 224 (112187) (2023).
[27] L. Christoffer, K.G. Anelia, K.G. Gueorgui, A perspective on thermal stability and mechanical properties of 2D Indium Bismide from ab initio molecular dynamics, Nanotechnology 33 (335706) (2022).
[28] S. Gianfranco, N. Giuseppe, G. Filippo, P. Béla, K.G. Gueorgui, K.G. Anelia, 2D graphitic-like gallium nitride and other structural selectivity in confinement at the graphene/SiC interface, CrystEngComm 25 (5810–5817) (2023).
[29] S. Plimpton, Fast parallel algorithms for short-range molecular dynamics, J. Comput. Phys. 117 (1) (1995) 1–19.
[30] J.-W. Jiang, Handbook of Stillinger-Weber potential parameters for two-dimensional atomic crystals, Intechopen, 2017.
[31] N. Martys, R. Mountain, Velocity Verlet algorithm for dissipativeparticle-dynamics-based models of suspensions, Phys. Rev. E 59 (3) (1999) 3733.
[32] J. Sun, Y. Li, Y. Karaaslan, C. Sevik, Y. Chen, Misfit dislocation structure and thermal boundary conductance of GaN/AlN interfaces, J. Appl. Phys. 130 (035301) (2021).
[33] N. Taormina, Y. Li, Y. Phillpot, Y. Chen, Effects of misfit dislocations and dislocation mobility on thermal boundary resistance of PbTe/PbSe interfaces, Comput. Mater. Sci. 235 (112828) (2024).
[34] Y. Li, Z. Zheng, A. Diaz, S. Pillpot, D. McDowell, Y. Chen, Resonant interaction between phonons and PbTe/PbSe (001) misfit dislocation networks, Acta Mater. 237 (118143) (2022).